

ARTICLE

<https://doi.org/10.1038/s41467-019-10872-z>

OPEN

Anoxygenic photosynthesis and the delayed oxygenation of Earth's atmosphere

Kazumi Ozaki ^{1,2,3,5}, Katharine J. Thompson⁴, Rachel L. Simister ⁴, Sean A. Crowe ^{1,4} & Christopher T. Reinhard^{1,2}

The emergence of oxygenic photosynthesis created a new niche with dramatic potential to transform energy flow through Earth's biosphere. However, more primitive forms of photosynthesis that fix CO₂ into biomass using electrons from reduced species like Fe(II) and H₂ instead of water would have competed with Earth's early oxygenic biosphere for essential nutrients. Here, we combine experimental microbiology, genomic analyses, and Earth system modeling to demonstrate that competition for light and nutrients in the surface ocean between oxygenic phototrophs and Fe(II)-oxidizing, anoxygenic photosynthesizers (photoferrotrophs) translates into diminished global photosynthetic O₂ release when the ocean interior is Fe(II)-rich. These results provide a simple ecophysiological mechanism for inhibiting atmospheric oxygenation during Earth's early history. We also find a novel positive feedback within the coupled C-P-O-Fe cycles that can lead to runaway planetary oxygenation as rising atmospheric pO₂ sweeps the deep ocean of the ferrous iron substrate for photoferrotrophy.

¹School of Earth and Atmospheric Sciences, Georgia Institute of Technology, Atlanta, GA 30332, USA. ²NASA Astrobiology Institute, Alternative Earths Team, Riverside, CA, USA. ³NASA Postdoctoral Program, Universities Space Research Association, Columbia, MD 21046, USA. ⁴Departments of Microbiology & Immunology and Earth, Ocean, & Atmospheric Sciences, University of British Columbia, Vancouver, BC V6T 1Z3, Canada. ⁵Present address: Department of Environmental Science, Toho University, Funabashi, Chiba 274-8510, Japan. Correspondence and requests for materials should be addressed to C.T.R. (email: chris.reinhard@eas.gatech.edu)

The large-scale oxygenation of Earth's atmosphere ~2.3 billion years ago (Ga) signaled one of the most profound biogeochemical shifts in Earth's history^{1,2}, and occurred as a direct result of photosynthetic oxygen production. It is widely assumed that the ubiquity of water as an electron donor for oxygenic photosynthesis would have conferred an enormous competitive advantage to the first oxygenic phototrophs, facilitating their rapid domination of the photosynthetic niche following their emergence^{3,4}. Paradoxically, evidence for oxygenic photosynthesis can be found as much as a billion years before the first large-scale oxygenation of Earth's atmosphere^{5–7}, and atmospheric O₂ has remained well below the present atmospheric level (PAL) for as much as ~90% of Earth's history^{1,8,9}. Evidence from Earth's rock record thus suggests a protracted interval of low-oxygen atmospheric chemistry following the evolution of the oxygen-evolving complex in the first oxygenic phototrophs.

Prior to the emergence of oxygenic photosynthesis, the photosynthetic niche would have been populated exclusively by anoxygenic phototrophs^{10,11}. Today, anoxygenic phototrophs proliferate in sunlit anoxic environments where they utilize a wide-range of electron donors including dihydrogen, hydrogen sulfide, thiosulphate, elemental sulfur, and ferrous iron [Fe(II)]¹². Ferrous iron would have been the most widely available electron donor for anoxygenic photosynthesis throughout much of Earth's early history^{13–22}, but the birth of the oxygen-evolving complex in the ancestors of extant cyanobacteria would have created a new photosynthetic niche decoupled from the supply of Fe(II) to illuminated surface ocean waters. This would have initiated fierce competition for light and bioessential elements—most importantly phosphorus (P)^{23–27}.

In modern aquatic environments, phototrophs compete for available light energy, introduced at the sea surface and attenuated with depth, and dissolved nutrients, largely mixed upward via advection and turbulent diffusion²⁸. As a result, organisms that are adapted to low light intensities can compete more effectively for nutrients introduced from deeper in the water column. In the modern ocean and many lakes, for example, low-light-adapted phytoplankton inhabit deep chlorophyll maxima, where they exploit nutrient supplies from below, make large contributions to primary production, and strongly diminish nutrient fluxes to the upper photic zone²⁹.

Anoxygenic phototrophs are especially well adapted to grow at low light levels, using specialized pigments to effectively harness light in spectral regions not commonly available to oxygenic phototrophs^{30,31}. Extant anoxygenic phototrophs—including facultatively anoxygenic cyanobacteria, Chlorobi, Chloroflexi, and purple bacteria—commonly position themselves below oxygenic cyanobacteria and algae, where they gain access to inorganic electron donors like reduced sulfur species and ferrous iron [Fe(II)]^{11,32,33}. Residing deeper in the photic zone, modern anoxygenic phototrophs are known to support appreciable primary production^{34,35}, while weakening the upward fluxes of reduced species and the supply of nutrients to overlying oxygenic cyanobacteria and algae. In particular, members of the Chlorobi are almost ubiquitously better adapted to low light levels than extant oxygenic cyanobacteria^{36,37}. Indeed, they photosynthesize at the lowest light levels recorded³⁷, and have the metabolic capacity to grow at low light through photoferrotrophy³⁵.

Collectively, these observations based on the physiology, ecology, and modes of extant photosynthesis imply that early anoxygenic phototrophs, growing through photoferrotrophy in Fe-rich (ferruginous) oceans, may have out-competed primitive oxygenic phototrophs for upwelling nutrients²³. As a first attempt to quantify the effects of this ecophysiological competition on the Earth system, we combine laboratory physiological experiments, genomics, a local reactive transport framework, and global biogeochemical cycle modeling. We find that competition for light and nutrients between different photosynthetic metabolisms represents a critically important feature of Earth's global O₂ cycle, modulating biospheric O₂ release and atmospheric oxygen when the ocean interior is Fe(II)-rich. Model sensitivity analysis indicates that the basic dynamics of this competition are robust to a wide range of values for key metabolic parameters. These results, combined with observations from the rock record and genomic constraints on the antiquity of phosphorus metabolism, suggest that this control should have been operative for the vast majority of Earth's history.

Results

P uptake potential and its antiquity in a model photoferrotroph. The first step in our approach involves a series of experiments to map the metabolic potential of the model pelagic photoferrotroph *Chlorobium phaeoferrooxidans* strain KB01, isolated from Kabuno Bay, East Africa³⁵. We find that during incubation experiments in the presence of dissolved Fe(II) and phosphate (PO₄³⁻), KB01 grows rapidly and draws down media PO₄³⁻ while photosynthetically oxidizing Fe(II) (Fig. 1), clearly showing robust growth at very low (nM) concentrations of inorganic P. Notably, we find that KB01 continues to grow and oxidize Fe(II) after dissolved PO₄³⁻ concentrations have decreased to asymptotic values below 4 nM, suggesting that KB01 can access Fe-bound PO₄³⁻ for growth (Fig. 1b).

We also find metabolic potential for the uptake of PO₄³⁻ at low concentrations in KB01's genome sequence. KB01 possesses genes that code for the high-affinity PO₄³⁻ uptake system (Pst—phosphate-specific transport) belonging to the *pho* regulon, which is induced by phosphorus scarcity and is used in extant marine cyanobacteria to mitigate P starvation^{38–40}. In KB01, the *pho* regulon is distributed across multiple contigs with redundancy at multiple locations within the genome (Fig. 2). The genome of KB01 also comprises genes that code for an array of enzymes used in P assimilation, breakdown, and recycling under P starved conditions, including alkaline phosphatases and polyphosphate kinases^{41,42} (Supplementary Table 1). Combined with the relatively low light requirements for photosynthesis in *Chlorobium* spp., the metabolic potential for P uptake and growth that

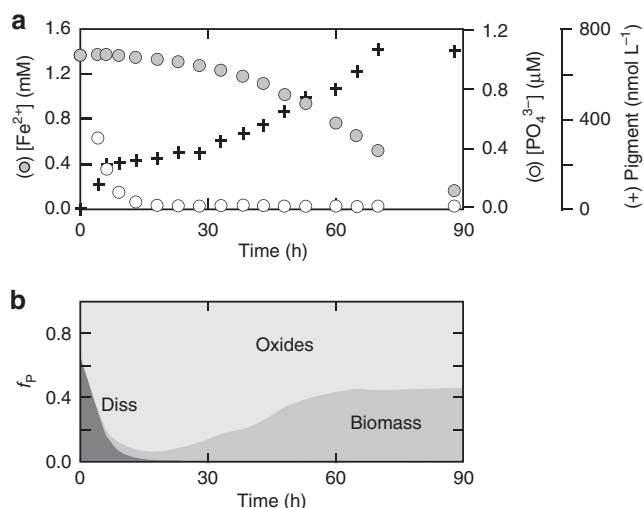


Fig. 1 Physiological data for *Chlorobium phaeoferrooxidans* str. KB01. **a** Time-series data for dissolved phosphate (O), dissolved ferrous iron (●), and pigment concentrations (+) in batch culture. **b** Time-series data for the partitioning of phosphorus between dissolved PO₄³⁻ (diss), Fe-oxide-bound phosphorus (oxides), and phosphorus in photosynthetic biomass (biomass)

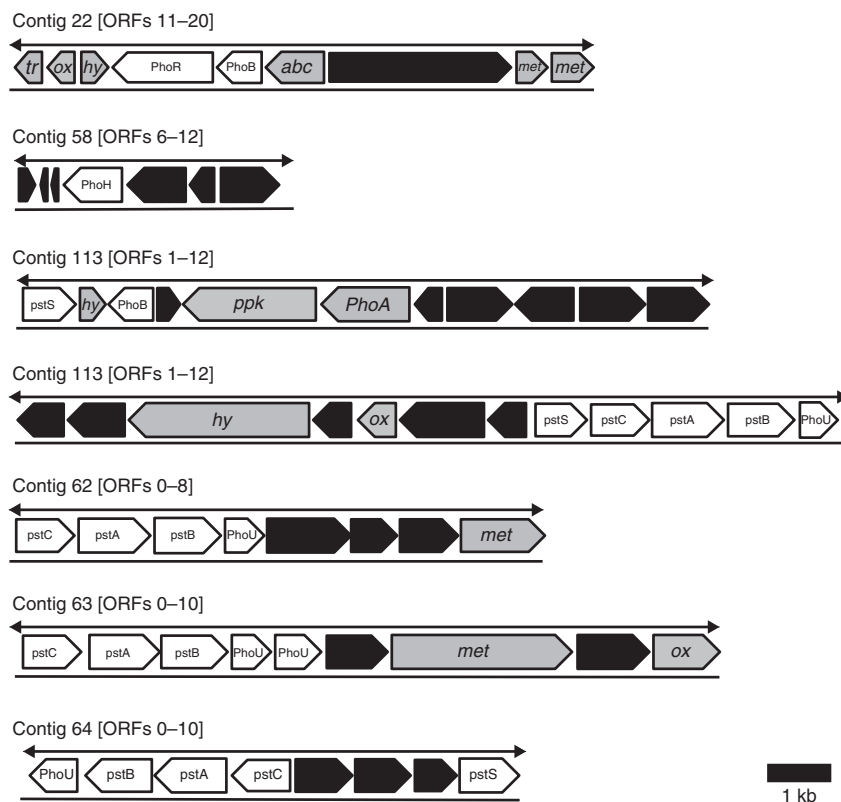


Fig. 2 Phosphorus gene positions in the genome of *Chlorobium phaeoferrooxidans* strain KB01. Highlighted are the positions of genes involved in high-affinity inorganic phosphorus (P_i) uptake (white), including components of the *pho* regulon, alkaline phosphatase (*PhoA*), and polyphosphate kinase (*ppk*). Also shown are positions of transcriptional regulator and transposase proteins (*tr*), membrane, envelope, and transporter proteins (*met*), hydrolases (*hy*), oxidoreductases (*ox*), ABC transporter proteins (*abc*), and other proteins (black) in each open-reading frame (ORF). kb kilobase

KB01 displays under low-P conditions suggests that pelagic photoferotrophs, as represented by KB01, should be effective competitors for available P in an Fe-rich water column setting with mixed modes of photosynthetic growth.

As a direct test for the antiquity of high-affinity PO_4^{3-} metabolism in the Chlorobiales, we compare phylogenies of components of the *pho* regulon against highly conserved 16S rRNA gene phylogenies (Fig. 3). A phylogenetic analysis of concatenated PstABC protein sequences, encoding three subunits of the trans-membrane PO_4^{3-} permease, reveals nearly identical branching patterns to those of the 16 rRNA gene, which implies vertical inheritance of the high-affinity PO_4^{3-} -uptake system in the Chlorobiales. By extension, this also suggests that the last common ancestor of crown group Chlorobiales likely had similar capacity for PO_4^{3-} metabolism to extant members like strain KB01. Phylogenies of PhoU, which regulates intracellular PO_4^{3-} metabolism, are also broadly congruent with the 16 rRNA gene phylogeny, providing further support for conserved, vertically inherited PO_4^{3-} metabolism in the Chlorobiales.

1-D ecosystem-biogeochemical model. To explore the potential impact of pelagic photoferotrophs on nutrient cycling within the photic zone, we embed idealized oxygenic phototrophic and photoferotrophic organisms in a 1-D advection–diffusion–reaction model meant to represent a generalized photic zone in a ferruginous ocean. Based on well-established models from environmental microbiology and our experimental work with KB01, we specify a simple form of competition between photoferotrophs and oxygenic phototrophs in which photoferotrophic growth is parameterized as a function of ambient

light, dissolved Fe(II), and nutrient P, while oxygenic phototrophic growth is constrained by both light and dissolved nutrients (see the “Methods” section). Light availability is assumed to vary with depth according to a simple exponential (*e*-folding) decay with a specified attenuation length scale. Iron can also be oxidized by dissolved O_2 , the kinetics of which are specified as a function of ambient $[O_2]$, $[Fe^{2+}]$, pH, temperature, and salinity according to ref. 43. Scavenging and co-precipitation of inorganic PO_4^{3-} onto/into Fe-oxide mineral phases occurs according to a simple distribution coefficient (K_d^{FeP}). Default values for our photic ecology model are given in Supplementary Table 2.

Representative results of our 1-D competitive photosynthesis model are shown in Fig. 4. Because pelagic photoferotrophs can compete effectively for P at low light levels (i.e., more deeply in the water column), they can strongly attenuate the flux of P to the oxygenic component of the photosynthetic community (Fig. 4a). This results in an emergent tiering pattern in which photoferotrophs outcompete oxygenic phototrophs for available P until dissolved Fe(II) is exhausted, after which P can break through to shallower oxygenic phototrophs (Fig. 4b). A particularly salient result of our model is the importance of the ratio of Fe(II) to PO_4^{3-} in deepwater ($[Fe/P]_d$) in controlling the relative importance of oxygenic phototrophs to overall system productivity (f_{oxy} ; Fig. 4c). Above a critical $[Fe/P]_d$ value, pelagic photoferotrophs effectively eliminate oxygenic phototrophs from the ecosystem by outcompeting them for nutrient P deep within the water column. In contrast, at lower $[Fe/P]_d$ photoferotrophs become progressively Fe(II)-limited, and oxygenic phototrophs garner a larger fraction of the photosynthetic niche.

Our principal results are relatively insensitive to the metabolic parameters of the model, and are robust across the range of

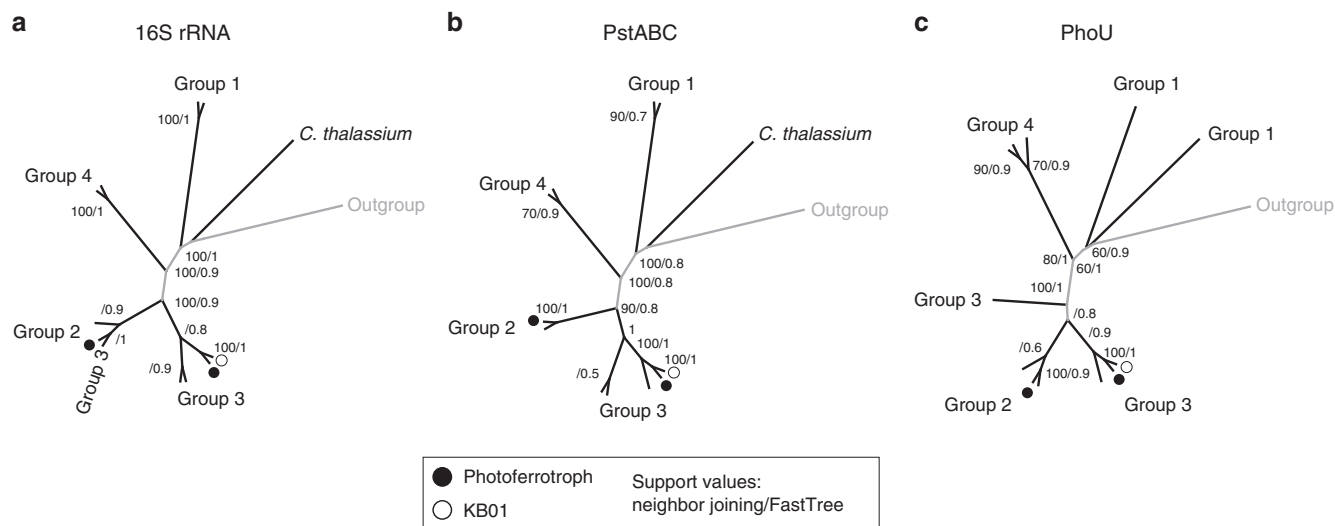


Fig. 3 Comparative molecular phylogeny of 16S rRNA and major genes regulating P metabolism. Approximately Maximum-Likelihood Trees (FastTree) of concatenated 16S rRNA gene (**a**), PstABC (**b**), and PhoU (**c**). Nodes are annotated with Neighbor Joining (1000x bootstrapped) and FastTree support values. These phylogenies are equivalent to previously established and accepted phylogenies for the Chlorobiales based on the 16S and FMO genes. Maximum likelihood and maximum parsimony yielded trees with similar topology (trees not shown). Clade nomenclature follows recommended taxonomy: Group 1 = *Prostheochloris*, Group 2 = *Chlorobium* 2, Group 3 = *Chlorobium* 3, Group 4 = *Chlorobaculum*. The outgroup is *Rhodothermus marinus* DSM 4252. Circles at the branch tips represent photoferotrophic organisms and the (○) denotes *Chlorobium phaeoferrooxidans* strain KB01. Note that *C. thalassium* lacks a PhoU gene

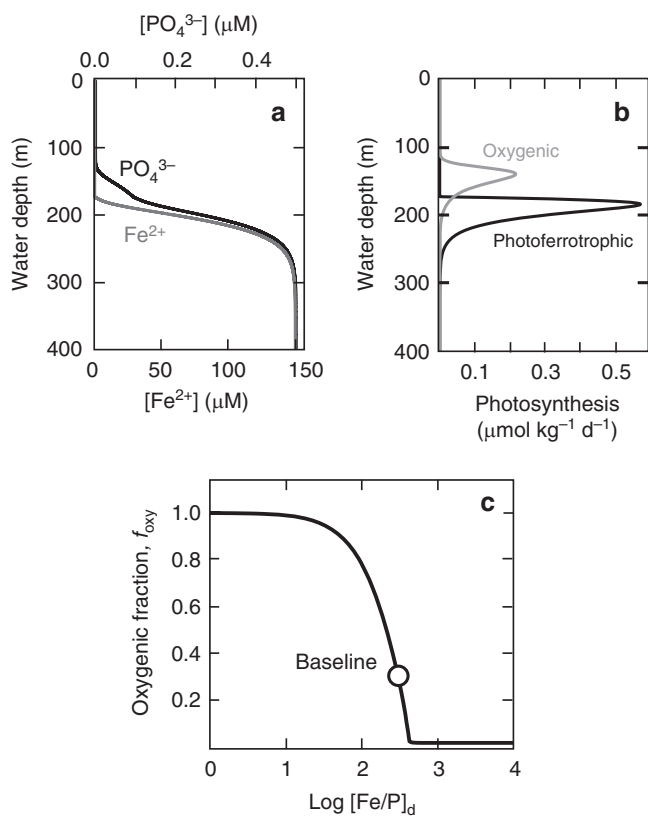


Fig. 4 Representative results from our 1-D competitive photosynthesis model. **a** Water column PO_4^{3-} and Fe^{2+} concentrations; and **b** rates of oxygenic and anoxygenic (photoferotrophic) photosynthesis for our baseline simulation. **c** Relative contribution of oxygenic photosynthesis to total water column photosynthesis (f_{oxy}) as a function of deep water dissolved Fe/P ratio. The open circle denotes our baseline simulation. Note the log scale in **c**

physical parameter values realistic for natural environments (Fig. 5). In particular, varying the key metabolic parameters of our model by as much as an order of magnitude above and below our default values has a small impact on our results (Fig. 5a). In addition, there is no a priori reason to expect that the basic ecophysiological phenomenon underlying our results—effective photoferotrophic consumption of nutrients at low light levels—has changed dramatically over time through the course of microbial evolution (see below). Our conclusions are thus most strongly dependent on the physical parameters used in the model. For example, relative oxygenic phototrophy can be increased appreciably relative to our default simulation by decreasing light penetration (e.g., increasing λ ; Fig. 5b), increasing rates of mixing due to eddy diffusion (K_e ; Fig. 5c), or decreasing upwelling rates (w ; Fig. 5e). However, in all of these cases the values required to markedly impact our default oxygenic productivity are very extreme relative to natural surface ocean settings^{44–49}. In addition, these changes could be easily offset by reasonable increases²³ in the distribution coefficient for P scavenging (K_d ; Fig. 5c), which will be regulated at any given period of Earth’s history by seawater concentrations of dissolved Si, Ca, and Mg. We thus consider the basic framework implied by our water column ecology model to be very robust to reasonable variability in both metabolic and physical parameters.

Global ocean-sediment biogeochemical model: CANOPS-KB.

In order to explore the potential large-scale impacts of competitive ecophysiology on Earth’s oxygen cycle, we employ an Earth system model (ESM) of the coupled C–N–P–O₂–S cycles. Our model, CANOPS-KB (see the “Methods” section), has a general and robust circulation scheme that is capable of producing well-resolved distributions of ¹⁴C and temperature and has been extensively tested and validated against observations from the modern and ancient Earth^{50,51}. The biogeochemical scheme is based on a primary limiting nutrient, phosphate (PO_4^{3-}), that ultimately controls biological productivity in the surface ocean, and includes biological productivity in the low-latitude

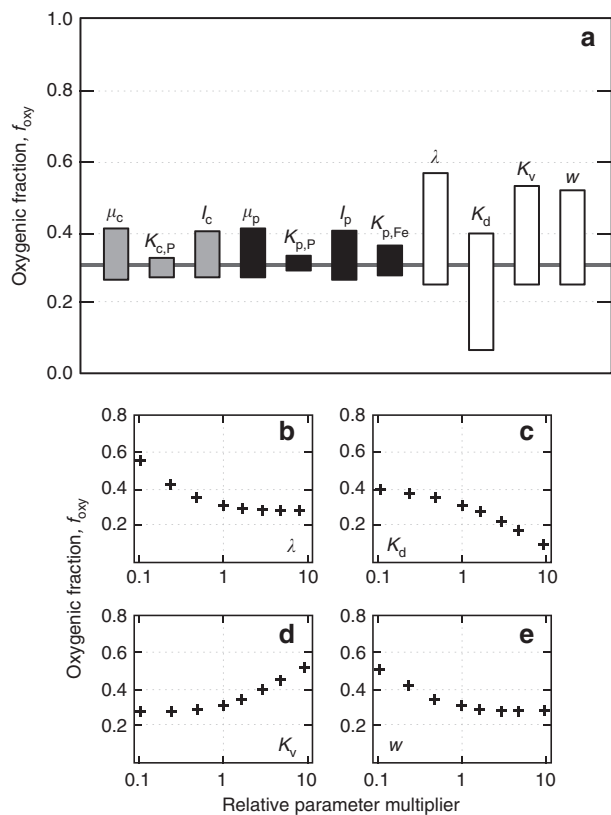


Fig. 5 Sensitivity analysis of the 1-D competitive photosynthesis model. Shown in **a** is the response of our principle diagnostic parameter, the fraction of overall photosynthesis performed by oxygenic phototrophs (f_{oxy}), to varying each metabolic and physical parameter of the model by an order of magnitude above and below the value in the default parameter set (shown by the black horizontal line and denoted by the open circle in Fig. 4). Major metabolic parameters are maximum growth rates (μ_i) and half-saturation constants for light (I_i) and nutrients ($K_{i,P}$) for oxygenic phototrophs and photoferrotrophs (subscripts c and p, respectively). Physical parameters include light attenuation constant (λ), distribution coefficient for scavenging/coprecipitation of phosphorus on iron oxides (K_d), eddy diffusivity (K_v), and upwelling rate (w). Shown in **b–e** are sensitivity ensembles for physical parameters, with relative oxygenic phototrophy plotted as a function of relative forcing of each parameter

and high-latitude surface ocean, a series of respiratory pathways in the ocean interior (aerobic respiration, denitrification, and sulfate reduction), secondary redox reactions (nitrification and aerobic sulfide oxidation), and the deposition, processing, and burial of organic matter and phosphorus in marine sediments. We also include redox-dependent scavenging (and subsequent burial) of phosphorus by Fe oxides building on previous work²⁷ (see the “Methods” section), and ecological competition between photoferrotrophs and oxygenic photosynthesizers based on a simplified version of our 1-D water column model (see the “Methods” section).

By specifying atmospheric O_2 , external inputs of P, and the ratio between dissolved Fe(II) and PO_4^{3-} in the deep ocean ($[Fe/P]_d$), we can use the model to compute the global burial rate of organic carbon originating from oxygenic phototrophs—and thus estimate the overall production of O_2 by the biosphere on geologic timescales. We can then combine this with an estimation of O_2 sinks due to inputs of volcanic/metamorphic reductants and oxidative weathering (the latter of which scales with

atmospheric O_2 ; see the “Methods” section) to calculate the net O_2 balance at Earth’s surface (Φ_{ox}). When biospheric O_2 production fluxes (i.e., the burial of organic carbon produced by oxygenic phototrophs) and consumption fluxes due to weathering and volcanic/metamorphic inputs are equal ($\Phi_{ox} = 0$), the global O_2 cycle is in equilibrium (open/closed circles in Fig. 6a). When $\Phi_{ox} > 0$ the biosphere is releasing O_2 at rates that exceed available sink fluxes, and atmospheric O_2 should rise. Similarly, when $\Phi_{ox} < 0$ consumption rates are greater than rates of production by the oxygenic biosphere, and atmospheric O_2 should fall.

We can also use this analysis to evaluate the stability of a given equilibrium point⁵². For example, if the slope at equilibrium is negative (open circle in Fig. 6a), there is negative feedback and the equilibrium point will be relatively stable to external perturbation. Conversely, if the slope at equilibrium is positive (closed circle in Fig. 6a), there is positive feedback and the equilibrium point should be unstable. The gradient of the slope indicates the overall stability at equilibrium. It is important to bear in mind that our analysis specifies $[Fe/P]_d$ as a boundary condition, while in reality we should expect this parameter to scale in some fashion with ocean–atmosphere O_2 abundance. This scaling is currently unknown and awaits more comprehensive knowledge of the coupled Fe–P–C–S– O_2 cycles in pervasively anoxic oceans. Nevertheless, we consider this approach useful for exploring the role of anoxygenic photosynthesis in the stability of Earth’s oxygen cycle.

Our stability analysis of the Earth surface oxygen cycle including competitive phototrophy yields two key insights. First, the location of stable equilibria depends strongly on $[Fe/P]_d$ —for example, for our benchmark model (with $[Fe/P]_d = 100$ and no external reductant flux) there is a stable equilibrium point at an atmospheric pO_2 value of $\sim 2 \times 10^{-3}$ atm, or $\sim 1\%$ PAL (open circle in Fig. 6a). However, the pO_2 value that yields a stable equilibrium scales directly with $[Fe/P]_d$ (Fig. 6b), such that higher $[Fe/P]_d$ yields lower pO_2 and vice versa. This effect can be further modulated by changes in external volcanic/metamorphic reductant fluxes. For example, the pO_2 corresponding to stable equilibrium drops to ~ 0.3 – 0.4% PAL in our benchmark model if we impose an external reductant flux of 3 Tmol O_2 equivalents year⁻¹ (Fig. 6a), on the low end of estimated volcanic/metamorphic reductant fluxes to modern Earth surface environments⁵³.

Second, our analysis predicts a threshold $[Fe/P]_d$ value below which the system will undergo runaway oxygenation (Fig. 6b). In our benchmark model this occurs at $[Fe/P]_d$ of ~ 20 , below which enhanced nutrient fluxes allow oxygenic phototrophs to oxygenate the photic zone, suppressing photoferrotrophic activity and phosphorus scavenging by iron oxides, promoting eutrophication of the ocean interior, and further enhancing nutrient fluxes to oxygenic phototrophs. Such a runaway oxygenation could occur as a result of increasing oceanic P or through a sufficient long-term drop in reductant flux. The stable pO_2 value also becomes highly sensitive to $[Fe/P]_d$ when $[Fe/P]_d > 200$ (Fig. 6b), with relatively small changes in $[Fe/P]_d$ causing large changes in the pO_2 at which stable equilibrium is possible. By contrast, in our nominal model $[Fe/P]_d$ values approaching ~ 400 strongly suppress the activity of oxygenic phototrophs. Although our model does not currently include the photochemical reaction network linking molecular oxygen (O_2), ozone (O_3), and methane (CH_4) in the atmosphere^{54,55}, it is anticipated that such a strong suppression of the activity of the oxygenated biosphere would tip the system into a runaway deoxygenation and result in a stable, reducing atmosphere (Fig. 6b).

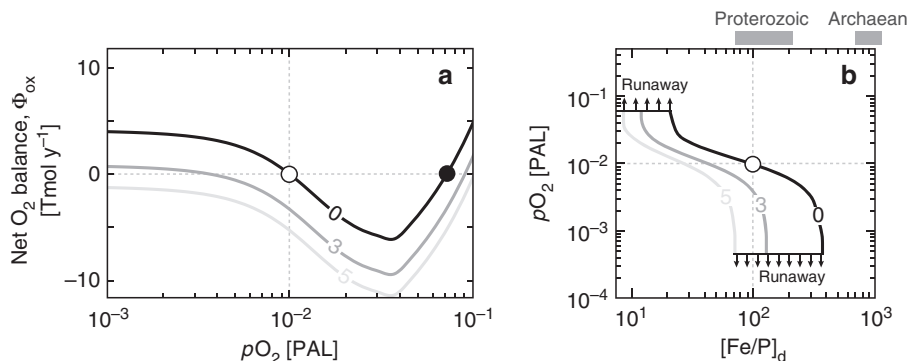


Fig. 6 Representative results from our global ocean-sediment biogeochemical model (CANOPS-KB). **a** Each curve shows net oxygen fluxes (Φ_{ox}) as a function of atmospheric pO_2 . Intersection points at $\Phi_{ox} = 0$ indicate regions of parameter space in which the O_2 cycle is at equilibrium and dominated by negative feedback (negative slope) and positive feedback (positive slope). Circles plotted along the black curve thus show examples of stable (open) and unstable (closed) equilibrium points for model runs at a nominal deep ocean Fe/P ratio of 100. Each curve is labeled by an assumed external reductant flux (i.e., volcanic/metamorphic reductant input minus O_2 accumulation due to hydrogen escape and/or imbalances in global S and Fe cycling, Φ_{red}) in Tmol O_2 equivalents year $^{-1}$. **b** Each curve plots stable equilibrium pO_2 values as a function of deep ocean Fe/P ratio ($[Fe/P]_d$) under the same conditions as shown in **a**. The (O) shows our nominal model ($[Fe/P]_d = 100$ and no external reductant input). Arrows above and below the curves denote regions where our model predicts runaway oxygenation or deoxygenation, respectively. Also shown in **b** are approximate estimates of $[Fe/P]_d$ for the Archean and Proterozoic (shaded gray bars; see text)

Discussion

We argue that strain KB01 represents a strong physiological analog to the ancestral photoferrotophs that would have populated ferruginous Precambrian oceans. The ecological prominence of the Chlorobiales in many modern analog environments implies that they are well adapted to growth and proliferation under conditions relevant to Precambrian marine environments⁵⁶. At the same time, the deep ancestry of the Chlorobiales implies that the genetic underpinning of this physiology has been conserved across billions of years—as is the case for N-fixation⁵⁶. While it is challenging to connect relative antiquity implied from sequence analyses (Fig. 3) to absolute age dates that can be tethered to the geologic record, biomarkers diagnostic of ancestral Chlorobiales have been recovered from 1.6 Ga shales⁵⁷, while molecular clocks imply emergence of stem group Chlorobi as early as the Mesoarchaeon⁵⁸. This implies that our results are likely applicable to the Mesoarchaeon or earlier and are almost certainly relevant to periods of Earth's history subsequent to the early Paleoproterozoic.

In addition to nutrient metabolism⁵⁶ (see above), both pigment biosynthesis pathways¹⁰ and accessory components of low-light photosystems⁵⁹ are strongly conserved within photosynthetic lineages. For example, the Fenna–Mathews–Olson (FMO) complex, which mediates energy transfer from chlorosomes to the photosynthetic reaction center and is unique to the Chlorobiales⁶⁰, is phylogenetically and functionally conserved^{59,61}, suggesting it was likely present in the last common ancestor of crown group Chlorobiales. The relative antiquity of the FMO complex and its role in bridging chlorosomes to the reaction center, which confers exceptional light harnessing capacity to the Chlorobiales, thus implies that the last common ancestor of crown group Chlorobiales was very well adapted to growth under low-light conditions and that this capacity emerged in stem group photosynthetic Chlorobi as early as the Mesoarchaeon⁵⁸, or possibly earlier. In addition, photoferrotophy by ancestral members of other photosynthetic lineages could also have played a similar ecological role and indeed high affinity PO_4^{3-} -uptake systems are broadly distributed across the bacteria⁶². Taken as a whole, sequence information, the ecology of extant Chlorobiales, and the geologic record all support the antiquity of the nutrient and light metabolism displayed by strain KB01.

The dynamics of our large-scale biogeochemical model depend strongly on the abundances of dissolved Fe and P in the ocean interior during Archean and Proterozoic time, which are not well-constrained at present. Nevertheless, we can obtain a basic sense of the links between our model and evolving ocean chemistry from constraints derived from laboratory experiments, thermodynamic calculations, and observations from the rock record. Recent estimates^{63,64} based largely on the hypothesis of a metastable green rust phase as a primary Fe mineral in Precambrian marine systems place Archean dissolved Fe on the order of $\sim 100 \mu\text{mol kg}^{-1}$, with Proterozoic dissolved Fe roughly an order of magnitude lower⁶⁴. These estimates are broadly consistent with the observation of siderite in Archean carbonate platforms⁶⁵ and the long-term thermodynamic stability of Fe-silicate phases in Archean seawater⁶⁶, though values for the Proterozoic could have been considerably higher than this if the formation of Fe-bearing carbonate and silicate phases was kinetically inhibited¹⁶.

If we combine these values for dissolved Fe(II) with estimates of deep ocean P concentration based on the P/Fe ratios observed in iron-rich chemical sediments deposited during the Archean and Proterozoic²³, we obtain $[Fe/P]_d$ values for the Archean of roughly 700–2000 and Proterozoic values around an order of magnitude below this. Interpreted in the context of our model, these values would imply an essentially anoxic Archean atmosphere despite the presence of oxygenic phototrophs in the surface oceans (Fig. 6b). We find that this is true even with no additional reductant flux from volcanic/metamorphic gases—an important observation given that proposed mechanisms for the first widespread oxygenation of Earth surface environments at ~ 2.3 Ga (the Great Oxidation Event, or GOE) overwhelmingly gravitate toward the role of geophysical O_2 sinks^{67–72}. Our results thus clearly demonstrate the importance of microbial physiology and deep ocean chemistry as controls on atmospheric O_2 and highlight the previously unrecognized role of deep ocean Fe:P ratios as a potential throttle on the timing and intensity of the GOE.

Furthermore, these estimates would yield a largely stable low-oxygen atmosphere during the Proterozoic according to our model (Fig. 6b). Uncertainties in both reductant fluxes from the solid Earth and deep ocean chemistry prevent us from definitively assigning any particular simulation to specific intervals of Proterozoic time, and it remains possible that ocean–atmosphere O_2

levels were variable throughout this interval as a function of time-dependent changes in rates of volcanism, ocean [Fe/P]_d values, and other factors. However, the *p*O₂ stability range in our model under roughly Proterozoic conditions is consistent with observations from the rock record, including the Fe/Mn chemistry of ancient weathering profiles^{73–75} and the stable isotope compositions of iron-rich chemical sediments⁷⁶, shales⁷⁷, and marine evaporite minerals^{74,78}. Other estimates placing Proterozoic *p*O₂ at higher values^{79–81} are also broadly consistent with our model^{82,83}, which may provide a mechanism that would allow a range of stable atmospheric oxygen levels encompassing existing geochemical estimates, as well as transitions between these levels on relatively short time scales. In any case, taken together with the apparent predominance of Fe(II)-rich conditions in the ocean interior throughout the Precambrian^{13,22,84}, our results implicate competition between different modes of photosynthesis as important in regulating the oxygen cycle during large intervals of Earth's history.

In summary, our coupled experimental-modeling results suggest an important role for competitive ecophysiology, modulated by changes in deep ocean chemistry, in controlling Earth's surface O₂ cycle. More specifically, we provide a simple biological mechanism for preventing atmospheric oxygenation in the face of sustained photosynthetic O₂ production during the Archean Eon and for explaining low atmospheric *p*O₂ during the Proterozoic Eon. We also find a potential positive feedback within the coupled C–P–O–Fe cycles that can lead to runaway planetary oxygenation, as rising atmospheric *p*O₂ sweeps the deep ocean of the ferrous iron substrate for photoferrotrophy, stimulates expansion of the oxygenic component of the photosynthetic biosphere, and causes atmospheric *p*O₂ to rise further. Future advances in quantitatively constraining ocean–atmosphere chemistry will help to pinpoint the external forcings required to initiate this runaway oxygenation, and definitively establish the conditions under which a similar runaway deoxygenation might occur. Nevertheless, our results demonstrate the fundamental importance of photosynthetic ecology and deep ocean Fe:P ratios for Earth system evolution.

Methods

Metabolic potential of *C. phaeoferrooxidans* strain KB01. *C. phaeoferrooxidans* strain KB01 was grown in medium adapted from ref. ⁸⁵, where potassium phosphate was replaced with potassium chloride. 0.6 mM Si was added to the medium and the ferrous iron concentration was 1.4 mM. The growth medium was inoculated with *C. phaeoferrooxidans* strain KB01 that had been previously grown on medium containing 4 mM phosphate. To limit P carryover through the inoculum, it was first centrifuged (5 min at 16,100 rcf) and the supernatant discarded prior to introduction to the P-free medium. Once inoculated, radiolabeled phosphate (³²P) was added to each bottle so that the final phosphate concentration was ~1.5 μM with radiation levels of 2 mCi.

To assess growth and P uptake kinetics, time points were taken every 3–5 h for 88 h. Subsamples were collected at each time point for iron speciation, pigment analysis, total radioactivity, dissolved radioactivity, radioactivity incorporated into the biomass, and radioactivity bound to ferric iron particles or cellular biomass. The iron speciation measurements were conducted using the ferrozine assay⁸⁶, while the pigments were extracted using a 7:2 methanol:acetone mixture⁸⁷. The sample for dissolved radioactivity was measured after filtration to 0.2 μm by scintillation counting of 1 mL of filtrate, while the total radioactivity was measured without filtration. The ³²P incorporated into biomass was determined by centrifuging 0.5 mL of sample for 5 min at 16,100 rcf, discarding the supernatant, and then treating with dithionite for 15 min to remove particulate iron and associated P. After treating with dithionite, the samples were centrifuged again for 5 min at 16,100 rcf, supernatant was discarded and 1 mL of iron-free media (no phosphate and containing 0.6 mM Si) was added to the sample, which was then counted. The ³²P sorbed to particles in solution was counted by treating 0.5 mL of sample with 1 mL of dithionite for 15 min. 0.5 mL of iron-free media (no phosphate and 0.6 mM Si) was then added to the sample and 1 mL of this was filtered to remove biomass and counted.

To determine metabolic potential for PO₄³⁻ metabolism in photoferrotrophic Chlorobiales, we searched the previously annotated genome of strain KB01 for genes known and implicated in microbial responses to P-starvation. The protein

identities were confirmed with a BLAST⁸⁸ search against the NCBI non-redundant database. Recovered genes were placed into their broader genomic context by searching for the host contig and recovering adjacent genes. The evolutionary history of PO₄³⁻ metabolism in the Chlorobiales was assessed through comparative phylogenetic analyses of the proteins PstA, PstB, and PstC, in a concatenated matrix, as well as PhoU, versus the 16S rRNA gene. Sequences were aligned using ClustalX2.1⁸⁹, and phylogenetic trees constructed with multiple methods (Neighbor Joining, FastTree, and verified with maximum likelihood and maximum parsimony). Tree nodes are labeled with both bootstrap (Neighbor Joining) and FastTree support values.

1-D water column model of competitive photosynthesis. Our 1-D water column model solves an advection–diffusion–reaction equation of the form:

$$\frac{\partial C}{\partial t} = w \frac{\partial C}{\partial z} - K_v \frac{\partial C}{\partial z^2} + \sum R_i, \quad (1)$$

where *C* represents dissolved concentrations (e.g., Fe²⁺, PO₄³⁻), *z* is depth, *w* is advection velocity (e.g., upwelling rate), *K_v* represents a diapycnal eddy diffusivity, and *R_i* denotes a series of kinetic reaction terms that control a given dissolved species in the water column. The equation is solved via finite-difference techniques using the R package ReacTran⁹⁰.

Our model specifies a simple form of competition between photoferrotrophs and oxygenic photosynthesizers based qualitatively on our experimental work with *C. phaeoferrooxidans* str. KB01. Photoferrotrophic growth is parameterized as a function of ambient light availability, dissolved ferrous iron levels, and dissolved nutrients (e.g., PO₄³⁻), while cyanobacterial growth is constrained by both light and dissolved nutrients:

$$J_{\text{photoferro}} = \mu_p \cdot \frac{I_z}{I_p + I_z} \cdot \frac{[\text{Fe}^{2+}]}{K_{p,\text{Fe}} + [\text{Fe}^{2+}]} \cdot \frac{[\text{PO}_4^{3-}]}{K_{p,\text{P}} + [\text{PO}_4^{3-}]}, \quad (2)$$

$$J_{\text{cyano}} = \mu_c \cdot \frac{I_z}{I_c + I_z} \cdot \frac{[\text{PO}_4^{3-}]}{K_{c,\text{P}} + [\text{PO}_4^{3-}]}, \quad (3)$$

where *μ_i* and *K_i* terms represent maximum growth rates and nutrient half-saturation constants for each photosynthetic metabolism, *I_i* terms represent light half-saturation constants for each photosynthesizer, and *I_z* represents light availability at a given depth in the water column. Light availability is assumed to vary with depth according to a simple exponential decay:

$$I_z = I_0 e^{-\lambda z}, \quad (4)$$

where *I₀* represents incident light at the surface, *z* represents depth, and *λ* represents an attenuation length-scale.

Inorganic oxidation of dissolved Fe²⁺ with O₂ proceeds according to:

$$J_{\text{ox}} = k_{\text{ox}} [\text{Fe}^{2+}] [\text{O}_2] [\text{OH}^-]^2, \quad (5)$$

where the kinetic rate constant is a function of temperature (*T*) and ionic strength (*s*) following ref. ⁴³:

$$\log k_{\text{ox}} = \left[21.56 - \frac{1545}{T} \right] - 3.29s^{0.5} + 1.52s_1, \quad (6)$$

Finally, scavenging and co-precipitation of inorganic PO₄³⁻ onto/into Fe-oxide mineral phases occurs according to a simple distribution coefficient (*K_d^{FeP}*). All default model parameters are given in Supplementary Table 2.

Global ocean-sediment biogeochemical model: CANOPS-KB. We employ a 1-D (vertically resolved) transport–reaction model of marine biogeochemistry to explore the global impact of ecophysiological constraints on the coupled Earth surface C–N–P–O₂–S cycles. Our model, CANOPS-KB (Supplementary Fig. 1), is an improved version of the original CANOPS model developed by Ozaki and Tajika⁵¹, and subsequently modified by Reinhard et al. ²⁷. The details of base model configuration, parameterization and validation are described elsewhere^{27,51}, but here we outline the basic model structure and the modifications developed for this study.

The CANOPS framework has a general and robust circulation scheme that is capable of producing well-resolved distributions of circulation tracers (e.g., ¹⁴C and temperature). The diffusion–advection model of the global ocean is coupled with a biogeochemical model and a parameterized sediment model. The biogeochemical scheme is based on a primary limiting nutrient, phosphate (PO₄³⁻), that ultimately controls biological productivity in the surface ocean, and includes biological productivity in the low-latitude and high-latitude surface ocean, a series of respiratory pathways (aerobic respiration, denitrification, and sulfate reduction), secondary redox reactions (nitrification and aerobic sulfide oxidation), and deposition and burial of organic matter and phosphorus in marine sediments. We also include redox-dependent scavenging (and subsequent burial) of phosphorus by Fe oxides²⁷. The principal biogeochemical processes, formulations, and constants used in the model are summarized in Supplementary Tables 3–5, and the major process modifications are summarized here.

Ecological competition between photoferrotophs and oxygenic photosynthesizers in our large-scale model is informed by our metabolic experiments with *C. phaeoferrooxidans* str. KB01 and the results of our 1-D water column model. In the CANOPS-KB model, the total new production ($J_{\text{ex}}^{\text{total}}$, in mol C m⁻² year⁻¹) is assumed to be intrinsically phosphorus limited;

$$J_{\text{ex}}^{\text{total}} = \alpha \cdot h_m \cdot \varepsilon \cdot [\text{PO}_4^{3-}] \cdot \frac{[\text{PO}_4^{3-}]}{K_m^{\text{P}} + [\text{PO}_4^{3-}]}, \quad (7)$$

where α represents C/P stoichiometry of producers (=106), h_m is the surface layer depth, and ε is the efficiency factor for phosphorus uptake, and K_m^{P} denotes the Monod half-saturation parameter for phosphate-limited growth. In this study we assume that photosynthetic carbon fixation adheres to canonical Redfield stoichiometry (C:N:P = 106:16:1) and that the nitrogen required to sustain productivity is compensated by the activity of diazotrophs. The phosphate availability in the surface layer is explicitly calculated based on the riverine input, water transport via advection and diffusion, and biological production. New production of photoferrotophic biomass is determined by the relative availability of both Fe(II) and PO_4^{3-} . Under conditions of Fe-limited growth within the photoferrotophic community, any P remaining after complete consumption of Fe (II) can then be used by oxygenic photosynthesizers (e.g., cyanobacteria). Under P-limited photoferrotophic growth, all bioavailable phosphorus is consumed by photoferrotophs and the contribution of oxygenic photosynthesizers to new production is curtailed. We can express the rates of new production due to photoferrotophy and oxygenic photosynthesis in terms of the fluxes of particulate carbon exported from the euphotic zone (J_{ex} ; in mol C m⁻² year⁻¹) as follows:

$$J_{\text{ex}}^{\text{pfe}} = \min \left[\frac{J_{\text{Fe}}^{\text{up}}}{r_{\text{FeC}}}, J_{\text{ex}}^{\text{total}} \right], \quad (8)$$

$$J_{\text{ex}}^{\text{cyano}} = \begin{cases} J_{\text{ex}}^{\text{total}} - J_{\text{ex}}^{\text{pfe}} & : J_{\text{ex}}^{\text{pfe}} < J_{\text{ex}}^{\text{total}} \\ 0 & : J_{\text{ex}}^{\text{pfe}} = J_{\text{ex}}^{\text{total}} \end{cases}, \quad (9)$$

where pfe and cyano represent contributions due to photoferrotophs and oxygenic photosynthesizers (e.g., cyanobacteria), respectively, r_{FeC} represents the stoichiometric ratio between Fe and C attendant to photoferrotophy, and $J_{\text{Fe}}^{\text{up}}$ is the upward flux of Fe(II) to the photic zone via advection and turbulent diffusion given by

$$J_{\text{Fe}}^{\text{up}} = [\text{Fe}/\text{P}]_d \cdot J_{\text{P}}^{\text{up}}, \quad (10)$$

where the upward PO_4^{3-} flux, J_{P}^{up} , is given by

$$J_{\text{P}}^{\text{up}} = A_{j=1} \cdot w \cdot [\text{PO}_4^{3-}]_{j=1} + A_{j=1} \cdot K_v \cdot \left. \frac{\partial [\text{PO}_4^{3-}]}{\partial z} \right|_{z=h_m}, \quad (11)$$

for the low-mid latitude surface region, where w (m year⁻¹), K_v (m² year⁻¹) diffusivity (5000 m² year⁻¹), and areal fraction of the $j = 1$ layer to the surface area of low-mid latitude region, respectively. h_m (m) is the depth of the mixed layer.

The scavenging and co-precipitation of inorganic PO_4^{3-} onto/within Fe-oxide mineral phases (in terms of mol P m⁻² year⁻¹) is formulated according to a simple distribution coefficient (K_d^{FeP}):

$$J_{\text{scav}} = \begin{cases} \gamma \cdot K_d^{\text{FeP}} \cdot [\text{PO}_4^{3-}]_j \cdot J_{\text{Fe}}^{\text{up}} & \text{when } [\text{O}_2]_{j=1} < 1 \mu\text{M} \\ 0 & \text{when } [\text{O}_2]_{j=1} \geq 1 \mu\text{M} \end{cases}, \quad (12)$$

where γ denotes the ultimate burial efficiency of scavenged P. The activity of photoferrotophs (and scavenging) is specified to cease when the layer just below the surface layer ($j = 1$) becomes oxygenated.

Rates of oxidative weathering of organic matter. In order to explore the potential consequences of photoferrotophy for the stability of Earth's global oxygen cycle, we employ a simple parameterization of the rate of oxidative weathering of organic matter in the crust ($J_{\text{w}}^{\text{org}}$) as a function of atmospheric $p\text{O}_2$ according to:

$$\frac{J_{\text{w}}^{\text{org}}}{J_{\text{w},0}^{\text{org}}} = f_w \cdot \exp \left[-\sigma_{\text{org}}^1 \cdot \exp \left[-\sigma_{\text{org}}^2 \cdot \text{PAL} \right] \right] \quad (13)$$

where σ_{org}^i terms refer to fitting constants (here with values of 4 and 150, respectively), PAL refers to atmospheric $p\text{O}_2$ relative to the PAL, and $J_{\text{w},0}^{\text{org}}$ refers to the modern globally integrated organic carbon oxidation rate. This relationship is based on an approximate fit to results from a 1-D reaction-transport model of organic carbon weathering in the crust^{91,92}. We introduce a free parameter in Eq. (13), f_w , which expresses the effect of continental erosion rate on the global rate of oxidative weathering ($f_w = 1$ for the benchmark simulations presented in the Main Text). We also assume that the riverine P input flux and sediment accumulation rate at the seafloor (SR) scale in a linear fashion with f_w . We employ this method for simplicity but note that the location and overall stability of equilibrium $p\text{O}_2$ values will respond to some extent on the parameters employed in the reaction-transport model (Supplementary Fig. 2). However, the basic components of our argument remain unchanged.

Evaluating the exogenic oxygen budget. We can define a global redox budget (in O₂ equivalents) for the combined ocean-atmosphere system as:

$$\Phi_{\text{ox}} = \Phi_{\text{org}} - \Phi_{\text{weath}} - \Phi_{\text{red}} \quad (14)$$

where Φ_{ox} denotes the net redox flux balance within the ocean-atmosphere system, Φ_{org} denotes oxygen production through the burial of oxygenic photosynthetic biomass in marine sediments, Φ_{weath} denotes the consumption of O₂ from the atmosphere during the oxidative weathering of organic carbon in the crust, and Φ_{red} denotes the net input flux of reducing power via the combined effects of volcanic/metamorphic gas input^{53,93}, escape of hydrogen to space, and any redox imbalance within the S and Fe budgets.

In our default analysis of the O₂ budget we do not explicitly evaluate O₂ fluxes associated with the pyrite sulfur subcycle or hydrogen escape from the upper atmosphere^{67,94,95}. In the case of the pyrite sulfur subcycle, the isotope record of sedimentary sulfur-bearing minerals for most of Precambrian time is conventionally considered to suggest that effectively all sulfur entering the oceans was removed as a constituent of sedimentary pyrite. In this case, O₂ fluxes within the pyrite sulfur subcycle should be largely balanced on the longest timescales, though we note that the oxidative weathering of pyrite potential provides an additional stabilizing mechanism for Earth's O₂ budget⁹⁶ and that the volcanic outgassing of SO₂ and subsequent burial of pyrite may also make a non-trivial contribution to overall redox balance^{93,97}. The flux associated with H escape from the atmosphere is very small at present, but may have been significantly larger during periods of elevated atmospheric CH₄ levels, in particular during the Archean Eon. We can combine this flux with the input flux of reductants from the solid Earth, and consider this combined exogenic O₂ flux as part of the reductant flux boundary condition (Φ_{red}) discussed in the Main Text. However, we stress that the conceptual framework we present for Earth's oxygen cycle is a natural and robust consequence of the inclusion of photoferrotophy, and that this would not be altered by considering a more inclusive O₂ budget. Nevertheless, our results highlight the importance of time-dependent stability analysis of the exogenic O₂ cycle as an important topic for future work.

Data availability

All analytical data not given in the Supplementary Information are available on request.

Code availability

Code for the 1-D water column competitive photosynthesis model is written in R and is available on GitHub (<https://github.com/ChrisReinhard/photoferrotophy.R>). Code for the CANOPS-KB model is written in Fortran and is available from K.O. or C.T.R. upon reasonable request.

Received: 20 March 2018 Accepted: 28 May 2019

Published online: 09 July 2019

References

- Lyons, T. W., Reinhard, C. T. & Planavsky, N. J. The rise of oxygen in Earth's early ocean and atmosphere. *Nature* **506**, 307–315 (2014).
- Holland, H. D. Volcanic gases, black smokers, and the great oxidation event. *Geochim. Cosmochim. Acta* **66**, 3811–3826 (2002).
- Kopp, R. E., Kirschvink, J. L., Hilburn, I. A. & Nash, C. Z. The Paleoproterozoic snowball Earth: a climate disaster triggered by the evolution of oxygenic photosynthesis. *Proc. Natl Acad. Sci. USA* **102**, 11131–11136 (2005).
- Kirschvink, J. L. & Kopp, R. E. Palaeoproterozoic ice houses and the evolution of oxygen-mediating enzymes: the case for a late origin of photosystem II. *Philos. Trans. R. Soc. B-Biol. Sci.* **363**, 2755–2765 (2008).
- Crowe, S. A. et al. Atmospheric oxygenation three billion years ago. *Nature* **501**, 535–538 (2013).
- Planavsky, N. J. et al. Evidence for oxygenic photosynthesis half a billion years before the Great Oxidation Event. *Nat. Geosci.* **7**, 283–286 (2014).
- Buick, R. When did oxygenic photosynthesis evolve? *Philos. Trans. R. Soc. B-Biol. Sci.* **363**, 2731–2743 (2008).
- Reinhard, C. T., Olson, S. L., Schwieterman, E. W. & Lyons, T. W. False negatives for remote life detection on ocean-bearing planets: Lessons from the early Earth. *Astrobiology* **17**, 287–297 (2017).
- Kump, L. The rise of atmospheric oxygen. *Nature* **451**, 277–278 (2008).
- Xiong, J., Fischer, W. M., Inoue, K., Nakahara, M. & Bauer, C. E. Molecular evidence for the early evolution of photosynthesis. *Science* **289**, 1724–1730 (2000).
- Johnston, D. T., Wolfe-Simon, F., Pearson, A. & Knoll, A. H. Anoxygenic photosynthesis modulated Proterozoic oxygen and sustained Earth's middle age. *Proc. Natl Acad. Sci. USA* **106**, 16925–16929 (2009).
- Hohmann-Marriott, M. F. & Blankenship, R. E. Evolution of photosynthesis. *Annu. Rev. Plant Biol.* **62**, 515–548 (2011).

13. Planavsky, N. J. et al. Widespread iron-rich conditions in the mid-Proterozoic ocean. *Nature* **477**, 448–451 (2011).
14. Poulton, S. W., Fralick, P. W. & Canfield, D. E. Spatial variability in oceanic redox structure 1.8 billion years ago. *Nat. Geosci.* **3**, 486–490 (2010).
15. Sperling, E. A. et al. Statistical analysis of iron geochemical data suggests limited late Proterozoic oxygenation. *Nature* **523**, 451–454 (2015).
16. Derry, L. A. Causes and consequences of mid-Proterozoic anoxia. *Geophys. Res. Lett.* **42**, 8538–8546 (2015).
17. Walker, J. C. G. Was the Archean biosphere upside down? *Nature* **329**, 710–712 (1987).
18. Walker, J. C. G. The early history of oxygen and ozone in the atmosphere. *Pure Appl. Geophys.* **117**, 498–512 (1978).
19. Widdel, F. et al. Ferrous iron oxidation by anoxygenic phototrophic bacteria. *Nature* **362**, 834–836 (1993).
20. Kappler, A., Pasquero, C., Konhauser, K. O. & Newman, D. K. Deposition of banded iron formations by anoxygenic phototrophic Fe(II)-oxidizing bacteria. *Geology* **33**, 865–868 (2005).
21. Canfield, D. E., Rosing, M. T. & Bjerrum, C. Early anaerobic metabolisms. *Philos. Trans. R. Soc. B* **361**, 1819–1836 (2006).
22. Poulton, S. W. & Canfield, D. E. Ferruginous conditions: a dominant feature of the ocean through earth's history. *Elements* **7**, 107–112 (2011).
23. Jones, C., Nomosatryo, S., Crowe, S. A., Bjerrum, C. J. & Canfield, D. E. Iron oxides, divalent cations, silica, and the early earth phosphorus crisis. *Geology* **43**, 135–138 (2015).
24. Tyrrell, T. The relative influences of nitrogen and phosphorus on oceanic primary production. *Nature* **400**, 525–531 (1999).
25. Bjerrum, C. J. & Canfield, D. E. Ocean productivity before about 1.9 Ga ago limited by phosphorus adsorption onto iron oxides. *Nature* **417**, 159–162 (2002).
26. Planavsky, N. et al. The evolution of the marine phosphate reservoir. *Nature* **467**, 1088–1090 (2010).
27. Reinhard, C. T. et al. Evolution of the global phosphorus cycle. *Nature* **541**, 386–389 (2017).
28. Herbert, T. D. & Sarmiento, J. L. Ocean nutrient distribution and oxygenation: Limits on the formation of warm saline bottom water over the past 91 m.y. *Geology* **19**, 702–705 (1991).
29. Silsbe, G. M. & Malkin, S. Y. in *Aquatic Microbial Ecology and Biogeochemistry: A Dual Perspective* (eds Gilbert, P. M. & Kana, T. M.) 141–152 (Springer International Publishing, Springer Nature Switzerland AG 2016).
30. Van Gemerden, H. & Mas, J. in *Anoxygenic Photosynthetic Bacteria* (eds Blankenship, R. E., Madigan, M. T. & Bauer, C. E.) 49–85 (Springer-Verlag, Springer Nature Switzerland AG 1995).
31. Blankenship, R. E., Sadekar, S. & Raymond, J. In *Evolution of Primary Producers in the Sea* (eds Falkowski, P. G. & Knoll, A. H.) 22–33 (Elsevier, Burlington, MA 2007).
32. Cohen, Y., Jørgensen, B. B., Revsbech, N. P. & Poplawski, R. Adaptation to hydrogen sulfide of oxygenic and anoxygenic photosynthesis among cyanobacteria. *Appl. Environ. Microbiol.* **51**, 398–407 (1986).
33. Jørgensen, B. B., Cohen, Y. & Revsbech, N. P. Transition from anoxygenic to oxygenic photosynthesis in a microcoleus-chthonoplastes cyanobacterial mat. *Appl. Environ. Microbiol.* **51**, 408–417 (1986).
34. Overmann, J. in *Advances in Microbial Ecology* (ed. Jones, J. G.) 251–288 (Springer, Springer Nature Switzerland AG 1997).
35. Llíros, M. et al. Pelagic photoferritrophy and iron cycling in a modern ferruginous basin. *Nat. Sci. Rep.* **5**, 13803 (2015).
36. Overmann, J., Cypionka, H. & Pfennig, N. An extremely low-light-adapted green sulfur bacterium from the Black Sea. *Limnol. Oceanogr.* **37**, 150–155 (1992).
37. Manske, A. K., Glaeser, J., Kuypers, M. M. M. & Overmann, J. Physiology and phylogeny of green sulfur bacteria forming a monospecific phototrophic assemblage at a depth of 100 meters in the Black Sea. *Appl. Environ. Microbiol.* **71**, 8049–8060 (2005).
38. Rao, N. & Torriani, A. Molecular aspects of phosphate transport in *Escherichia coli*. *Mol. Microbiol.* **4**, 1083–1090 (1990).
39. Neidhardt, F. C. *Escherichia coli and Salmonella: Cellular and Molecular Biology*. (ASM Press, Washington, D.C. 1996).
40. Aguen, M. & Spira, B. Transcriptional processing of the pst operon of *Escherichia coli*. *Curr. Microbiol.* **58**, 264–267 (2009).
41. Adams, M. M., Gómez-García, M. R., Grossman, A. R. & Bhaya, T. Phosphorus deprivation responses and phosphonate utilization in a thermophilic *Synechococcus* sp. from microbial mats. *J. Bacteriol.* **190**, 8171–8184 (2008).
42. Lidbury, I. D. et al. The 'known' genetic potential for microbial communities to degrade organic phosphorus is reduced in low-pH soils. *Microbiol. Open* **6**, 4 (2017).
43. Millero, F. J., Sotolongo, S. & Izaguirre, M. The oxidation kinetics of Fe(II) in seawater. *Geochim. Cosmochim. Acta* **51**, 793–801 (1987).
44. Vaulot, D., Marie, D., Olson, R. J. & Chisholm, S. W. Growth of *Prochlorococcus*, a photosynthetic prokaryote, in the equatorial Pacific Ocean. *Science* **268**, 1480–1482 (1995).
45. Chavez, F. P. & Messie, M. A comparison of eastern boundary upwelling ecosystems. *Prog. Oceanogr.* **83**, 80–96 (2009).
46. Cloern, J. E. Turbidity as a control on phytoplankton biomass and productivity in estuaries. *Cont. Shelf Res.* **7**, 1367–1381 (1987).
47. Waterhouse, A. F. et al. Global patterns of diapycnal mixing from measurements of the turbulent dissipation rate. *J. Phys. Oceanogr.* **44**, 1854–1872 (2014).
48. Cronin, M. F., Pelland, N. A., Emerson, S. R. & Crawford, W. R. Estimating diffusivity from the mixed layer heat and salt balances in the North Pacific. *J. Geophys. Res.: Oceans* **120**, 7346–7362 (2015).
49. Decloedt, T. & Luther, D. S. On a simple empirical parameterization of topography-catalyzed diapycnal mixing in the abyssal ocean. *J. Phys. Oceanogr.* **40**, 487–508 (2010).
50. Ozaki, K., Tajima, S. & Tajika, E. Conditions required for oceanic anoxia/euxinia: Constraints from a one-dimensional ocean biogeochemical cycle model. *Earth Planet. Sci. Lett.* **304**, 270–279 (2011).
51. Ozaki, K. & Tajika, E. Biogeochemical effects of atmospheric oxygen concentration, phosphorus weathering, and sea-level stand on oceanic redox chemistry: implications for greenhouse climates. *Earth Planet. Sci. Lett.* **373**, 129–139 (2013).
52. Kump, L. R. Chemical stability of the atmosphere and ocean. *Palaeogeogr. Palaeoclimatol. Palaeoecol.* **75**, 123–136 (1989).
53. Catling, D. C. & Kasting, J. F. *Atmospheric Evolution on Inhabited and Lifeless Worlds* (Cambridge University Press, Cambridge, UK 2017).
54. Goldblatt, C., Lenton, T. M. & Watson, A. J. Bistability of atmospheric oxygen and the great oxidation. *Nature* **443**, 683–686 (2006).
55. Claire, M. W., Catling, D. C. & Zahnle, K. J. Biogeochemical modelling of the rise in atmospheric oxygen. *Geobiology* **4**, 239–269 (2006).
56. Thompson, K. J., Simister, R. L., Hahn, A. S., Hallam, S. J. & Crowe, S. A. Nutrient acquisition and the metabolic potential of photoferritrophic Chlorobi. *Front. Microbiol.* **8**, 1212 (2017).
57. Brocks, J. J. et al. Biomarker evidence for green and purple sulphur bacteria in a stratified Paleoproterozoic sea. *Nature* **437**, 866–870 (2005).
58. Magnabosco, C., Moore, K. R., Wolfe, J. M. & Fournier, G. P. Dating phototrophic microbial lineages with reticulate gene histories. *Geobiology* **16**, 179–189 (2018).
59. Alexander, B., Andersen, J. H., Cox, R. P. & Imhoff, J. F. Phylogeny of green sulfur bacteria on the basis of gene sequences of 16S rRNA and of the Fenna–Matthews–Olson protein. *Arch. Microbiol.* **178**, 131–140 (2002).
60. Blankenship, R. E., Olson, J. M. & Miller, M. In *Anoxygenic Photosynthetic Bacteria* (eds Blankenship, R. E., Madigan, M. T. & Bauer, C. E.) 399–435 (Kluwer, Springer Nature Switzerland AG 1995).
61. Valteau, S. et al. Absence of selection for quantum coherence in the Fenna–Matthews–Olson complex: a combined evolutionary and excitonic study. *ACS Cent. Sci.* **3**, 1086–1095 (2017).
62. Sowell, S. M. et al. Transport functions dominate the SAR11 metaproteome at low-nutrient extremes in the Sargasso Sea. *ISME J.* **3**, 93–105 (2009).
63. Halevy, I., Alesker, M., Schuster, E. M., Popovitz-Biro, R. & Feldman, Y. A key role for green rust in the Precambrian oceans and the genesis of iron formations. *Nat. Geosci.* **10**, 135–139 (2017).
64. Halevy, I. & Bachan, A. The geologic history of seawater pH. *Science* **355**, 1069–1071 (2017).
65. Holland, H. D. *The Chemical Evolution of the Atmosphere and Ocean*. (Princeton University Press, Princeton, NJ 1984).
66. Tosca, N. J., Guggenheim, S. & Pufahl, P. K. An authigenic origin for Precambrian greenalite: implications for iron formation and the chemistry of ancient seawater. *GSA Bull.* **128**, 511–530 (2015).
67. Catling, D. C., Zahnle, K. J. & McKay, C. P. Biogenic methane, hydrogen escape, and the irreversible oxidation of early life. *Science* **293**, 839–843 (2001).
68. Kump, L. R. & Barley, M. E. Increased subaerial volcanism and the rise of atmospheric oxygen 2.5 billion years ago. *Nature* **448**, 1033–1036 (2007).
69. Gaillard, F., Scaillet, B. & Arndt, N. T. Atmospheric oxygenation caused by a change in volcanic degassing pressure. *Nature* **478**, 229–232 (2011).
70. Lee, C. T. A. et al. Two-step rise of atmospheric oxygen linked to the growth of continents. *Nat. Geosci.* **9**, 417–424 (2016).
71. Chowdhury, P., Gerya, T. & Chakraborty, S. Emergence of silicic continents as the lower crust peels off on a hot plate-tectonic Earth. *Nat. Geosci.* **10**, 698–703 (2017).
72. Smit, M. A. & Mezger, K. Earth's early O₂ cycle suppressed by primitive continents. *Nat. Geosci.* **10**, 788–792 (2017).

73. Zbinden, E. A., Holland, H. D. & Feakes, C. R. The Sturgeon Falls paleosol and the composition of the atmosphere 1.1 Ga BP. *Precambrian Res.* **42**, 141–163 (1988).
74. Planavsky, N. J. et al. A case for low atmospheric oxygen levels during Earth's middle history. *Emerg. Top. Life Sci.* **2**, 149–159 (2018).
75. Babechuk, M. G., Kleinhanns, I. C. & Schoenberg, R. Chromium geochemistry of the ca. 1.85 Ga Flin Flon paleosol. *Geobiology* **15**, 30–50 (2016).
76. Planavsky, N. J. et al. Low Mid-Proterozoic atmospheric oxygen levels and the delayed rise of animals. *Science* **346**, 635–638 (2014).
77. Cole, D. B. et al. A shale-hosted Cr isotope record of low atmospheric oxygen during the Proterozoic. *Geology* **44**, 555–558 (2016).
78. Crockford, P. W. et al. Triple oxygen isotope evidence for limited mid-Proterozoic primary productivity. *Nature* **559**, 613–616 (2018).
79. Zhang, S. et al. Sufficient oxygen for animal respiration 1,400 million years ago. *Proc. Natl Acad. Sci. USA* **113**, 1731–1736 (2016).
80. Wang, X. et al. Oxygen, climate and the chemical evolution of a 1400 million year old tropical marine setting. *Am. J. Sci.* **317**, 861–900 (2017).
81. Blamey, N. J. F. et al. Paradigm shift in determining Neoproterozoic atmospheric oxygen. *Geology* **44**, 651–654 (2016).
82. Planavsky, N. J. et al. No evidence for high atmospheric oxygen levels 1,400 million years ago. *Proc. Natl Acad. Sci. USA* **113**, E2550–E2551 (2016).
83. Yeung, L. Y. Low oxygen and argon in the Neoproterozoic atmosphere at 815 Ma. *Earth Planet. Sci. Lett.* **480**, 66–74 (2017).
84. Canfield, D. E. et al. Ferruginous conditions dominated later neoproterozoic deep-water chemistry. *Science* **321**, 949–952 (2008).
85. Hegler, F., Posth, N. R., Jiang, J. & Kappler, A. Physiology of phototrophic iron (II)-oxidizing bacteria: implications for modern and ancient environments. *FEMS Microbiol. Ecol.* **66**, 250–260 (2008).
86. Stookey, L. L. Ferrozine—a new spectrophotometric reagent for iron. *Anal. Chem.* **42**, 779–781 (1970).
87. Ruivo, M. et al. Extraction and quantification of pigments in aerobic anoxygenic phototrophic bacteria. *Limnol. Oceanogr.: Methods* **12**, 338–350 (2014).
88. Altschul, S. F. et al. Gapped BLAST and PSI-BLAST: a new generation of protein database search programs. *Nucleic Acids Res.* **25**, 3389–3402 (1997).
89. Larkin, M. A. et al. Clustal W and Clustal X version 2.0. *Bioinformatics* **23**, 2947–2948 (2007).
90. Soetaert, K. & Meysman, F. Reactive transport in aquatic ecosystems: Rapid model prototyping in the open source software R. *Environ. Model. Softw.* **32**, 49–60 (2012).
91. Bolton, E. W., Berner, R. A. & Petsch, S. T. The weathering of sedimentary organic matter as a control on atmospheric O₂: II. Theoretical modeling. *Am. J. Sci.* **306**, 575–615 (2006).
92. Miyazaki, Y., Planavsky, N., Bolton, E. W. & Reinhard, C. T. Making sense of massive carbon isotope excursions with an inverse carbon cycle model. *J. Geophys. Res.: Biogeosci.* **123**, 2485–2496 (2018).
93. Ozaki, K., Reinhard, C. T. & Tajika, E. A sluggish mid-Proterozoic biosphere and its effect on Earth's redox balance. *Geobiology* **17**, 3–11 (2019).
94. Canfield, D. E. The early history of atmospheric oxygen: homage to Robert M. Garrels. *Annu. Rev. Earth Planet. Sci.* **33**, 1–36 (2005).
95. Kump, L. R. & Garrels, R. M. Modeling atmospheric O₂ in the global sedimentary redox cycle. *Am. J. Sci.* **286**, 337–360 (1986).
96. Johnson, A. C. et al. Experimental determination of pyrite and molybdenite oxidation kinetics at nanomolar oxygen concentrations. *Geochim. Cosmochim. Acta* **249**, 160–172 (2019).
97. Olson, S. L. et al. Volcanically modulated pyrite burial and ocean–atmosphere oxidation. *Earth Planet. Sci. Lett.* **506**, 417–427 (2019).

Acknowledgements

K.O. acknowledges support from the NASA Postdoctoral Program at the NASA Astrobiology Institute, administered by Universities Space Research Association under contact with NASA. K.O. also acknowledges JSPS KAKENHI Grant Number JP25870185. C.T.R. acknowledges support from the NASA Astrobiology Institute and the Alfred P. Sloan Foundation. This work was also supported by NSERC Discovery Grant 0487 to S.A.C. Steven Hallam, Aria Hahn, and Martin Hirst helped generate genomic data for strain KB01.

Author contributions

K.O., S.A.C., and C.T.R. designed the research. K.O., C.T.R., and S.A.C. designed and implemented the biogeochemical models. K.J.T. performed physiological and microbiological analysis of *C. phaeoferrooxidans* KB01. R.L.S., K.J.T., and S.A.C. performed genomic and phylogenetic analyses. All authors contributed to interpretation of the combined results and the writing of the manuscript.

Additional information

Supplementary Information accompanies this paper at <https://doi.org/10.1038/s41467-019-10872-z>.

Competing interests: The authors declare no competing interests.

Reprints and permission information is available online at <http://npg.nature.com/reprintsandpermissions/>

Peer review information: *Nature Communications* thanks Craig Moyer and other anonymous reviewer(s) for their contribution to the peer review of this work.

Publisher's note: Springer Nature remains neutral with regard to jurisdictional claims in published maps and institutional affiliations.



Open Access This article is licensed under a Creative Commons Attribution 4.0 International License, which permits use, sharing, adaptation, distribution and reproduction in any medium or format, as long as you give appropriate credit to the original author(s) and the source, provide a link to the Creative Commons license, and indicate if changes were made. The images or other third party material in this article are included in the article's Creative Commons license, unless indicated otherwise in a credit line to the material. If material is not included in the article's Creative Commons license and your intended use is not permitted by statutory regulation or exceeds the permitted use, you will need to obtain permission directly from the copyright holder. To view a copy of this license, visit <http://creativecommons.org/licenses/by/4.0/>.

© The Author(s) 2019